


SCIENTIFIC REPORTS



OPEN

Epitaxial growth of iridate pyrochlore $\text{Nd}_2\text{Ir}_2\text{O}_7$ films

J. C. Gallagher^{1,*}, B. D. Esser^{2,*}, R. Morrow³, S. R. Dunsiger⁴, R. E. A. Williams², P. M. Woodward³, D. W. McComb² & F. Y. Yang¹

Received: 14 December 2015

Accepted: 10 February 2016

Published: 29 February 2016

Epitaxial films of the pyrochlore $\text{Nd}_2\text{Ir}_2\text{O}_7$ have been grown on (111)-oriented yttria-stabilized zirconia (YSZ) substrates by off-axis sputtering followed by post-growth annealing. X-ray diffraction (XRD) results demonstrate phase-pure epitaxial growth of the pyrochlore films on YSZ. Scanning transmission electron microscopy (STEM) investigation of an $\text{Nd}_2\text{Ir}_2\text{O}_7$ film with a short post-annealing provides insight into the mechanism for crystallization of $\text{Nd}_2\text{Ir}_2\text{O}_7$ during the post-annealing process. STEM images reveal clear pyrochlore ordering of Nd and Ir in the films. The epitaxial relationship between the YSZ and $\text{Nd}_2\text{Ir}_2\text{O}_7$ is observed clearly while some interfacial regions show a thin region with polycrystalline Ir nanocrystals.

The 5d transition metal oxides have attracted much attention due to their strong spin-orbit coupling (SOC), which scales with Z^4 , where Z is the atomic number. Given such strong SOC, exotic phases of matter are predicted to occur, including the topological insulator, Weyl semimetal, and chiral spin liquid^{1–4}. Such materials have potential applications in quantum computing and spintronics⁵. The family of pyrochlore iridate compounds ($\text{A}_2\text{Ir}_2\text{O}_7$) are proving to be a promising arena within which to investigate these interesting phases. In some cases, the materials are geometrically frustrated, as the magnetic species occupy a network of corner sharing tetrahedra. The spin liquid phase has been observed in $\text{Pr}_2\text{Ir}_2\text{O}_7$ down to 0.3 K⁶, and there is evidence for the Weyl semimetal phase in Rh-doped $\text{Nd}_2\text{Ir}_2\text{O}_7$ ⁷ and $\text{Eu}_2\text{Ir}_2\text{O}_7$ ⁸. Theoretical studies have shown that the predicted topological insulator and Weyl semimetal phases can be induced by an all-in all-out spin structure of the rare earth (RE) pyrochlore iridates^{9,10}. In addition, there has been experimental observation of metal-to-insulator transitions in some RE pyrochlore iridates ($A = \text{Y}, \text{Nd}, \text{Sm}, \text{or Eu}$) at the same temperature as the magnetic ordering temperature^{9,11–13}.

Theoretical studies of the pyrochlore iridate thin films predict that the topological insulator and Weyl semimetal phases can be induced in the pyrochlores from epitaxial strain and finite size effects^{9,14} providing motivation to synthesize pyrochlore thin films. Previous research reports the synthesis of $\text{Bi}_2\text{Ir}_2\text{O}_7$ ¹⁵ and $\text{Eu}_2\text{Ir}_2\text{O}_7$ ¹⁶ thin films by pulsed laser deposition. In this paper, we report the synthesis of $\text{Nd}_2\text{Ir}_2\text{O}_7$ using off-axis magnetron sputtering with *ex situ* post-annealing.

Synthesis

Sputter Target Synthesis. Nd_2O_3 and IrO_2 powders were thoroughly mixed then ground for at least 2 hours in stoichiometric ratios with an excess of 5 mol% IrO_2 . The samples were pressed into a pellet, and placed in an alumina tube, which was sealed in an evacuated silica tube to prevent the iridium from volatilizing as the IrO_3 phase¹⁷ during heating before forming the ternary pyrochlore $\text{Nd}_2\text{Ir}_2\text{O}_7$ phase. This would cause the powder to be neodymium rich and lead to the formation of Nd_3IrO_7 or $\text{Nd}_6\text{Ir}_2\text{O}_{13}$ impurity phases (depending on the oxygen level)^{18,19}. After sealing in a silica tube, samples were heated for 160 hours at a temperature $T = 950^\circ\text{C}$ with a ramping rate of $1^\circ\text{C}/\text{min}$. Afterwards, the samples were taken out of the silica tubes and heated at $T = 1125^\circ\text{C}$ in pure O_2 at atmospheric pressure in a tube furnace for several days to volatilize the excess iridium away, leaving stoichiometric pyrochlore powders with a lattice constant of 10.373 \AA (see supplementary information for further analysis of the powder).

Thin Film Synthesis. The $\text{Nd}_2\text{Ir}_2\text{O}_7$ powder was pressed into a 2-inch sputtering target and used for ultra-high vacuum, off-axis magnetron sputtering. $\text{Nd}_2\text{Ir}_2\text{O}_7$ films were deposited on (111)-oriented 8 mol%

¹Department of Physics, The Ohio State University, Columbus, OH 43210, USA. ²Center for Electron Microscopy and Analysis, Department of Materials Science and Engineering, The Ohio State University, Columbus, OH 43212, USA. ³Department of Chemistry, The Ohio State University, Columbus, OH 43210, USA. ⁴Center for Emergent Materials, The Ohio State University, Columbus, OH 43210, USA. *These authors contributed equally to this work. Correspondence and requests for materials should be addressed to J.C.G. (email: gallagher.549@osu.edu)

O ₂ partial pressure effect (12 hour anneal at $T = 750^\circ\text{C}$)	
0.03 bar to 200 bar O ₂	Pure phase epitaxial pyrochlore Nd ₂ Ir ₂ O ₇ films
No O ₂ (Pure N ₂ or vacuum)	No Nd ₂ Ir ₂ O ₇ phase detected
Temperature effects (12 hour anneal at 1 bar of pure O ₂)	
$T \geq 775^\circ\text{C}$	Epitaxial Nd ₂ Ir ₂ O ₇ forms, but with an impurity phase at $2\theta \approx 29^\circ$ in XRD (possibly Nd ₃ IrO ₇ or Nd ₆ Ir ₂ O ₁₃)
$T = 750^\circ\text{C}$	Pure phase epitaxial pyrochlore Nd ₂ Ir ₂ O ₇ films
$T = 700^\circ\text{C}$	Pure phase epitaxial pyrochlore Nd ₂ Ir ₂ O ₇ films, though intensities of the pyrochlore XRD peaks are weaker and can be enhanced by further heating at 750°C
Annealing Time Effects (750°C in air)	
5 minutes	Nucleation of Epitaxial Nd ₂ Ir ₂ O ₇ crystallites of ~ 100 nm observed at YSZ interface [see Fig. 2(a)].
≥ 6 hours	Nd ₂ Ir ₂ O ₇ films are fully crystallized

Table 1. Summary of results of annealing amorphous Nd₂Ir₂O₇ films.

yttria-stabilized zirconia (YSZ) substrates in 12.5 mTorr of Ar + 1% O₂ atmosphere at room temperature. DC sputtering with a constant current of 60 mA was used, resulting in a deposition rate of 2 nm/minute. After the sputter deposition, the films were crystallized by annealing in atmospheric pressure N₂/O₂ mixture with oxygen partial pressures ranging from 30 mbar to 200 bar at 750°C for times ranging from 5 min to 50 hr with ramping rates of 0.5–1 $^\circ\text{C}/\text{min}$ above 500°C . Results showed that changing the oxygen partial pressure does not have an obvious effect on the crystal quality; however, annealing at higher temperatures ($\geq 775^\circ\text{C}$) results in the formation of the possible Nd₃IrO₇ or Nd₆Ir₂O₁₃ impurity phases. A summary of the effect of annealing under different conditions is shown in Table 1. Each film was analyzed with a Bruker D8 Discover triple-axis X-ray diffractometer. Figure 1(a) shows the synchrotron XRD scan of the Nd₂Ir₂O₇ powder converted to the Cu K _{α} wavelength for comparison with Fig. 1(b,c) showing the 2θ - ω XRD scans of a Nd₂Ir₂O₇ film, which only exhibit the (111)-series of the pyrochlore peaks, indicating a phase-pure, (111)-oriented pyrochlore film on YSZ. The out-of-plane lattice constant was calculated to be 10.387 Å for the Nd₂Ir₂O₇ film, which is close to the bulk value of 10.373 Å obtained from the synchrotron XRD data. The inset to Fig. 1(c) shows a rocking curve of the Nd₂Ir₂O₇ (222) peak which reveals a narrow peak with a full-width-at-half-maximum of 0.006° and a broad baseline possibly caused by inhomogeneity in the Nd₂Ir₂O₇ film.

Microscopy Analysis and Discussion. In order to study the early stages of the growth mechanism of Nd₂Ir₂O₇, an 800 nm Nd₂Ir₂O₇ film was deposited, followed by a 5-minute post-growth annealing at 750°C (with the same ramp rate specified above). High-angle annular dark field scanning transmission electron microscopy (HAADF-STEM) of the pyrochlore film was performed using an FEI probe-corrected Titan³ 80–300 S/TEM at 300 kV with a detector collection range of 55–375 mrad. Figure 2(a) shows a low magnification HAADF-STEM image of a cross-section of the annealed film. The film was predominantly amorphous with crystallites nucleated at the YSZ interface. Close examination reveals {111} and {001} faceted crystallites [Fig. 2(b)] surrounded by regions exhibiting dark contrast [Fig. 2(c)] in the HAADF image.

To fully understand the nature of the faceted crystals and Nd₂Ir₂O₇/YSZ interface, elemental analysis was performed by energy-dispersive X-ray (EDX) spectroscopy using the FEI Super-X quad-silicon drift detector system. An EDX profile across the crystalline/amorphous Nd₂Ir₂O₇ interface [Fig. 2(d)] was quantified using experimental Cliff-Lorimer k -factors obtained from the Nd₂Ir₂O₇ crystal assuming perfect 2:2:7 stoichiometry. This demonstrates that the as-deposited (amorphous) material was stoichiometric, which implies that the nanocrystals formed during the post-anneal. Note that spectra were collected at specimen orientations far from major crystallographic zone axes to minimize probe-channeling effects that could differ significantly between the amorphous and crystalline materials.

Films that had been post-annealed for significantly longer times (approximately 12 hours) were observed to be completely crystalline. Higher magnification HAADF-STEM images of the Nd₂Ir₂O₇/YSZ interface in these films [Fig. 3(a)] reveals an epitaxial relationship: $\langle 111 \rangle_{\text{Nd}_2\text{Ir}_2\text{O}_7} \parallel \langle 111 \rangle_{\text{YSZ}}$ and $\langle 110 \rangle_{\text{Nd}_2\text{Ir}_2\text{O}_7} \parallel \langle 110 \rangle_{\text{YSZ}}$. In HAADF-STEM or “Z-contrast” imaging, the intensity of an atomic column is approximately proportional to $Z^{1.8}$. As shown in Fig. 3(b,c), this contrast in the images of the Nd₂Ir₂O₇ film is characteristic of a high degree of pyrochlore ordering. The most intense atomic columns contain only Ir atoms ($Z = 77$), while the least intense contain only Nd ($Z = 60$), and the columns of intermediate contrast are alternating Nd and Ir atoms with 1:1 ratio.

In some regions of the Nd₂Ir₂O₇/YSZ interface, a thin “cloudy” layer was observed in the HAADF-STEM images, as shown in Fig. 4(a). This observation might be mis-interpreted as an amorphous layer at the interface between the YSZ and the Nd₂Ir₂O₇, but this would be inconsistent with the epitaxial relationship described above. In order to demonstrate that this epitaxial relationship remains despite the presence of the “cloudy” layer, the image in Fig. 4(a) was Fourier filtered to enhance the contrast from the crystalline materials. In the Fourier filtered image, the epitaxial relationship is clear [Fig. 4(b)], although the filtering process does reduce the Z-contrast and introduces mathematical artifacts around the edges of the image. HAADF-STEM images acquired from thinner TEM foils, Fig. 5(a), revealed nanocrystals, approximately 1–2 nm in diameter in the interfacial region. The nanocrystals exhibit a cubic crystal structure, with spatial frequencies in the fast Fourier Transform (FFT) that match the lattice parameter of metallic Ir [Fig. 5(b)] and are distinctly different from those of the Nd₂Ir₂O₇

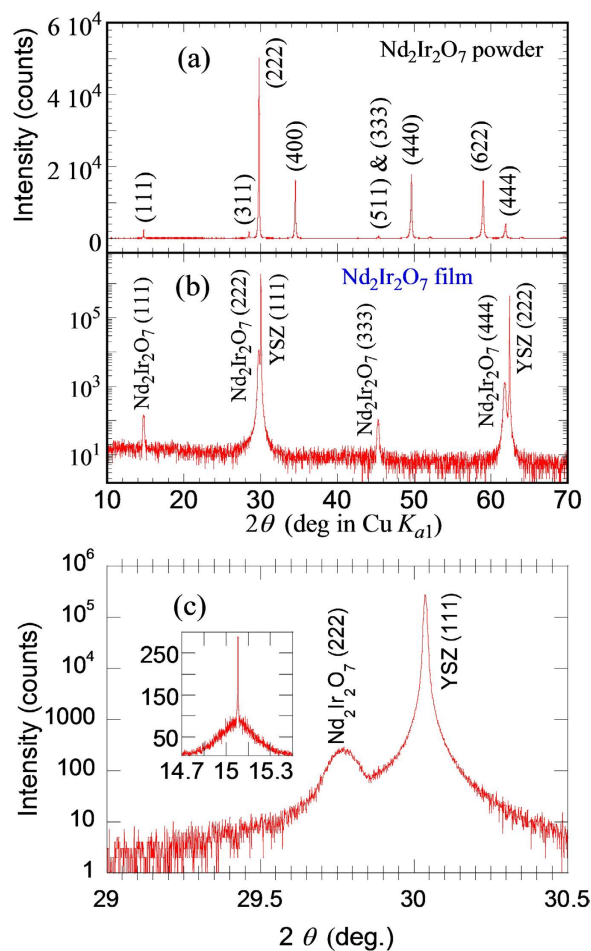


Figure 1. (a) $\theta/2\theta$ XRD scan of $\text{Nd}_2\text{Ir}_2\text{O}_7$ powders (taken at Argonne National Lab Advanced Photon Source using an X-ray wavelength of 0.413191 Å), which was converted to the Cu $K_{\alpha 1}$ wavelength of 1.5405 Å for comparison. (b) 2θ - ω XRD scan of a 200-nm thick $\text{Nd}_2\text{Ir}_2\text{O}_7$ film grown on YSZ (111). The sample was post-growth annealed at 750 °C in pure O_2 at atmospheric pressure with a ramp rate of 0.5 °C/min. (c) High resolution XRD scan of the same film around the YSZ (111) and $\text{Nd}_2\text{Ir}_2\text{O}_7$ (222) peaks. The inset is the rocking curve of the $\text{Nd}_2\text{Ir}_2\text{O}_7$ (222) peak, which consists of a narrow peak with full-width-at-half-maximum of 0.006° and a broad baseline.

film [Fig. 5(c)]. When the dark contrast observed at the triple junction of the YSZ substrate, amorphous $\text{Nd}_2\text{Ir}_2\text{O}_7$ and crystalline faceted $\text{Nd}_2\text{Ir}_2\text{O}_7$ noted in Fig. 2(b), is examined at higher magnification [Fig. 5(d)], it is observed that the Ir nanoparticles are also present [Fig. 5(e)].

The accumulation of Ir nanocrystals, specifically at the triple junction, can help explain the appearance of Ir metal in some regions of the interface but not others due to projection considerations in STEM imaging. It is reasonable to believe that the dark triple junction seen in Fig. 5(d) completely surrounds the base of the crystalline $\text{Nd}_2\text{Ir}_2\text{O}_7$ island [Fig. 6(a)]. Consequently, some areas of the TEM specimen near the interface may include partially the dark disordered region and partially crystalline $\text{Nd}_2\text{Ir}_2\text{O}_7$ along the electron beam path, resulting in a “cloudy” interface, as shown in Fig. 6(a–c).

It is clear that the nucleation and growth of crystalline $\text{Nd}_2\text{Ir}_2\text{O}_7$ films is influenced by multiple factors. During the annealing process, it is common in some systems for nucleation sites to form at all edges of the film and not exclusively at the interface, resulting in the formation of a polycrystalline thin film, such as the case for YSZ grown on sapphire²⁰. In other systems, nucleation sites at the interface grow epitaxially accompanied by the formation of a random polycrystalline film far from the interface, such as the case for $\text{YBa}_2\text{Cu}_3\text{O}_7$ films grown on SrTiO_3 with *ex situ* annealing²¹. YSZ is well lattice matched to $\text{Nd}_2\text{Ir}_2\text{O}_7$ and its cubic fluorite structure is a variant of the pyrochlore structure favoring the formation of nucleation sites exclusively at the interface with an epitaxial orientation. This potentially enables the entire film to be epitaxial as the nucleation sites grow by consuming the surrounding materials until the film is fully crystallized and the epitaxial orientation is well preserved. The curved surfaces that are apparent at the triple junctions [Figs 2(b) and 5(e)] are consistent with wetting phenomena suggesting liquid- or glassy-like behavior at the amorphous-crystalline interface at elevated temperatures. This is worth considering further as the nominal annealing temperature is well below the melting

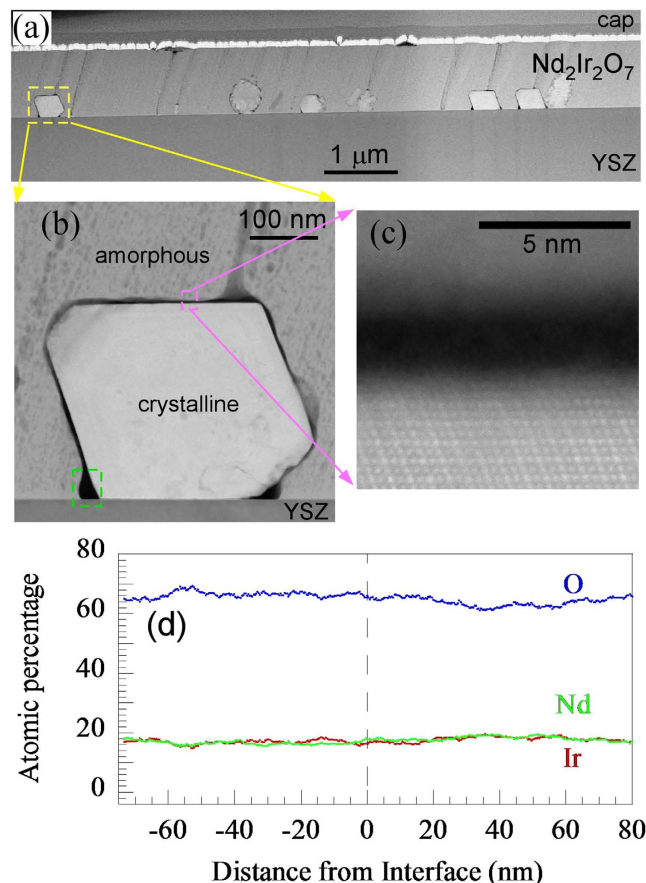


Figure 2. (a) STEM image of a Nd₂Ir₂O₇ film with 5 minute post-growth annealing reveals several Nd₂Ir₂O₇ crystallites nucleated at the YSZ interface. (b) STEM image of the left-most crystallite in (a) with facets along the {111} and {001} planes. (c) High magnification STEM image near the top of the crystallite in (b). The decrease in volume from the crystallization causes void regions to appear around the crystallite. (d) EDX spectra across the amorphous to crystalline transition region with the crystalline region on the right. There is no detected difference in stoichiometry between the regions.

temperature of Nd₂Ir₂O₇. We note that the crystallization of the pyrochlore phase is an exothermic reaction with an enthalpy of formation of 88.7 kJ/mol¹⁹. According to the Neumann–Kopp rule²² the heat capacity of Nd₂Ir₂O₇ is

$$C_p(\text{Nd}_2\text{Ir}_2\text{O}_7) = 2 C_p(\text{IrO}_2) + C_p(\text{Nd}_2\text{O}_3). \quad (1)$$

Previous research²³ has determined the heat capacity of IrO₂ to be

$$C_p(\text{J k}^{-1}\text{mol}^{-1}) = 87.6 + 6.20 \times 10^{-3} T - 7.80 \times 10^5 T^{-2} - 433 T^{-1/2}, \quad (2)$$

and Nd₂O₃ has been determined²⁴ to be

$$C_p(\text{J k}^{-1}\text{mol}^{-1}) = 117 + 28.1 \times 10^{-3} T - 1.26 \times 10^6 T^{-2}. \quad (3)$$

Eqs. (1–3) predict that the energy released from the crystallization could raise the temperature in the vicinity of the interface from 750 °C to about 1030 °C. This is above the decomposition temperature of IrO₂ of 1020 °C¹⁹, thus causing the formation of metallic Ir nanoparticles near the crystalline/amorphous interface. The high oxygen ion conductivity of YSZ, which peaks at 8 mol% Y₂O₃²⁵, may enhance the formation of Ir nanoparticles by creating an oxygen deficient interfacial layer. It may be possible to prevent such an interfacial layer by using a buffer material to block the oxygen flow to the substrate. In addition, it may be possible to prevent IrO₂ decomposition by annealing at lower temperatures; however, crystallizing Nd₂Ir₂O₇ at temperatures below 750 °C is challenging.

Conclusions

In summary, Nd₂Ir₂O₇ powders were synthesized in an evacuated silica tube and their structural properties were analyzed using laboratory as well as synchrotron X-ray diffraction. We report growth of Nd₂Ir₂O₇ epitaxial films using off-axis magnetron sputtering followed by post-annealing. XRD results demonstrate phase-pure epitaxial

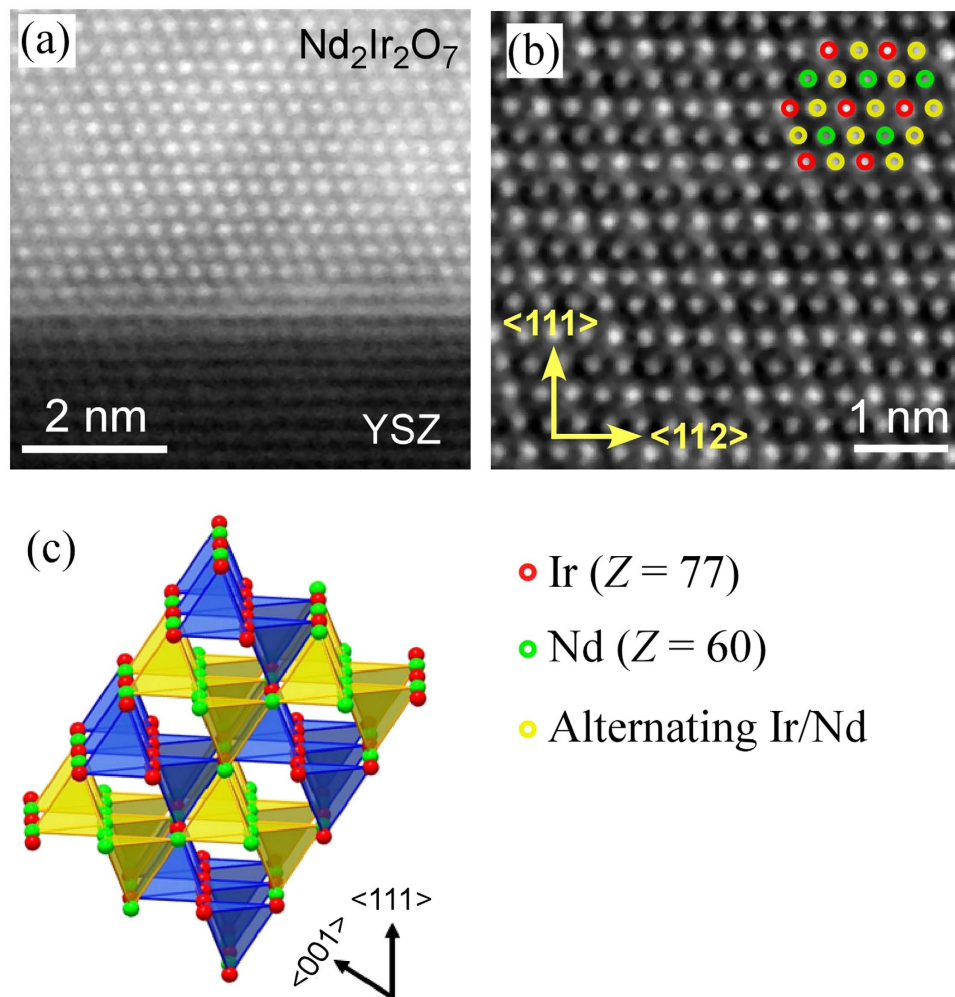


Figure 3. (a) STEM image of a $\text{Nd}_2\text{Ir}_2\text{O}_7$ film grown on YSZ (111) looking down the $\langle 110 \rangle$ axis. The $\text{Nd}_2\text{Ir}_2\text{O}_7$ film is ordered in pyrochlore structure and has an epitaxial relationship with the YSZ substrate. (b) High resolution STEM image of the $\text{Nd}_2\text{Ir}_2\text{O}_7$ film away from the interface shows the pyrochlore ordering of the Nd and Ir sublattices as schematically shown in (c).

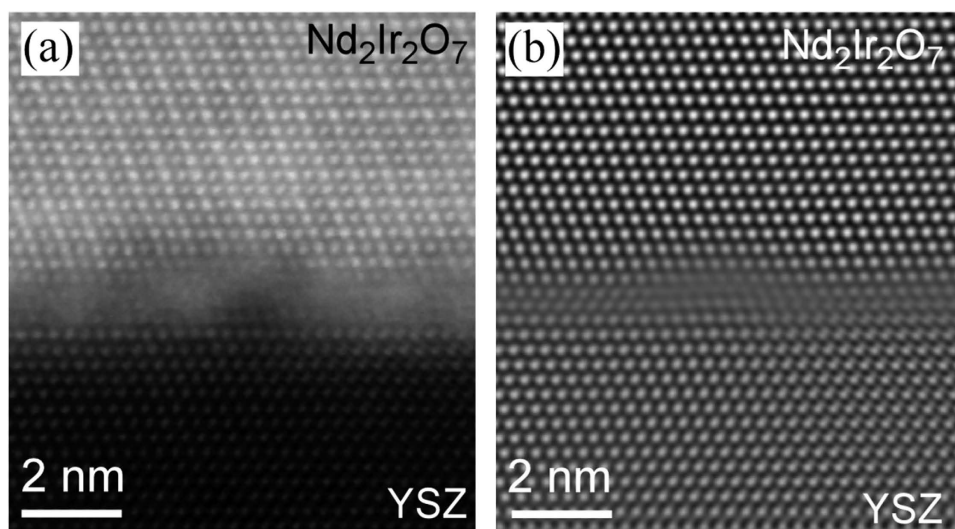


Figure 4. (a) STEM image revealing a “cloudy” interface in a region of the sample. (b) Fourier filtering of (a) reveals an epitaxial relationship at the interface despite the “cloudy” layer.

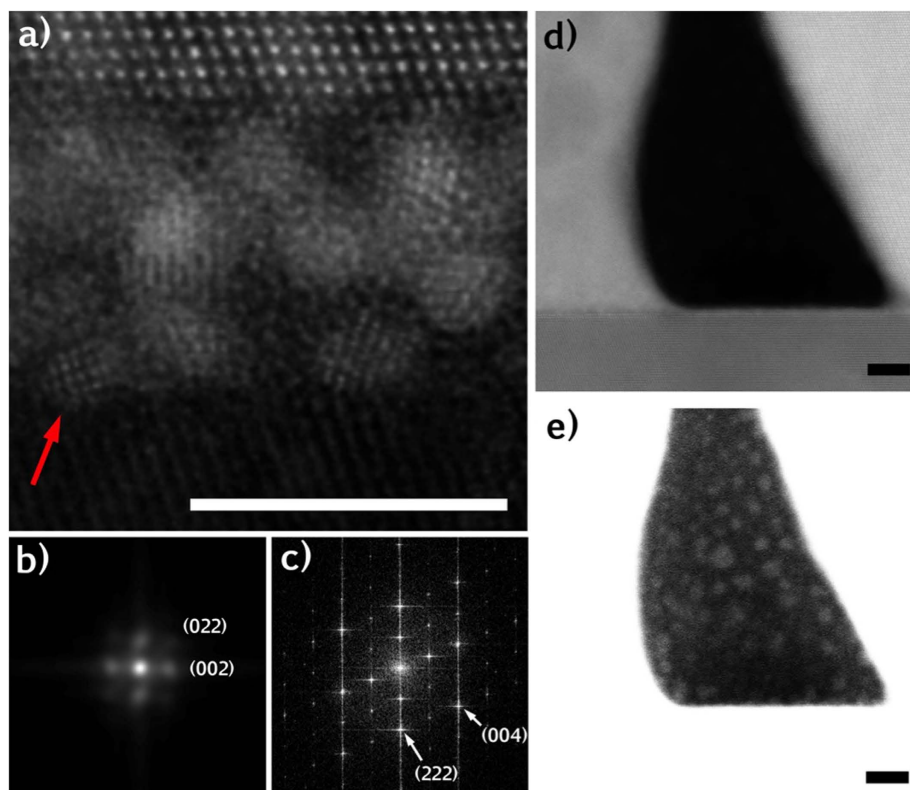


Figure 5. (a) High magnification STEM image of nanoparticles at the $\text{Nd}_2\text{Ir}_2\text{O}_7/\text{YSZ}$ interface. (b) FFT of the nanoparticle indicated by red arrow in (a) clearly indicates a cubic structure, with spatial frequencies matching the lattice parameter of metallic Ir, which is distinct from (c) the FFT of the pyrochlore $\text{Nd}_2\text{Ir}_2\text{O}_7$. (d) HAADF STEM image of the bottom-left corner of the island marked by the green box in Fig. 2(b). (e) A saturated image of (d) shows metallic Ir nanoparticles filling the void space at the island growth front. Scale bars on all images are 5 nm.

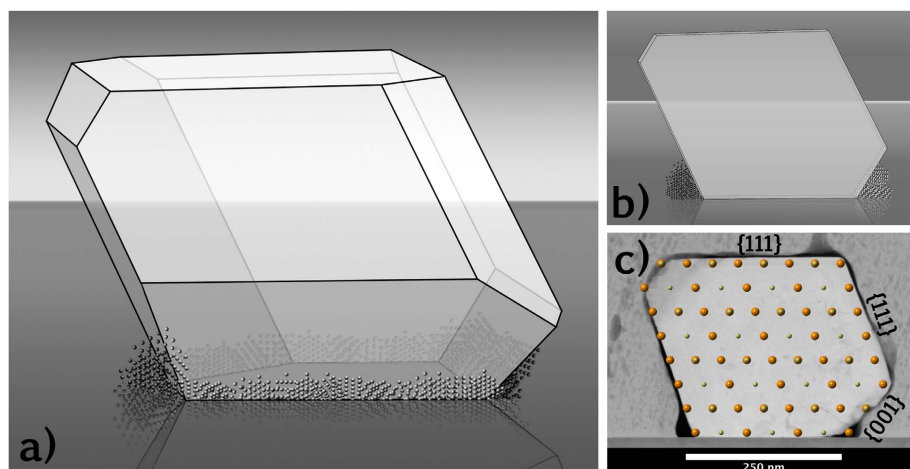


Figure 6. (a) Schematic of the crystallite shown in Fig. 2(b) assuming the crystallite forms facets primarily along $\{111\}$ and $\{001\}$ planes. Features at the $\text{Nd}_2\text{Ir}_2\text{O}_7/\text{YSZ}/\text{amorphous}$ triple junction represent Ir nanocrystals. (b) Schematic of the sample after being sliced into a $\langle 110 \rangle$ TEM foil with Ir nanocrystals visible only at the edges. (c) STEM image of crystallite with a schematic of the pyrochlore structure overlaid on the crystallite and the miller indices of the facets labeled. This confirms the crystal facets primarily on $\{111\}$ planes, but also on $\{001\}$ planes.

films grown on YSZ (111). HAADF-STEM images reveal clear pyrochlore ordering. Additionally, $\text{Nd}_2\text{Ir}_2\text{O}_7$ grows by the formation of epitaxial nucleation sites exclusively at the YSZ interface that slowly absorb the surrounding amorphous material forming a (111)-oriented crystalline film.

References

- Witczak-Krempa, W., Chen, G., Kim, Y. B. & Balents, L. Correlated Quantum Phenomena in the Strong Spin-Orbit Regime. *Annu. Rev. Condens. Matter Phys.* **5**, 57–82 (2014).
- Huang, S.-M. *et al.* A Weyl Fermion semimetal with surface Fermi arcs in the transition metal monpnictide TaAs class. *Nat. Commun.* **6**, 7373 (2015).
- Bendt, G. *et al.* Deposition of topological insulator Sb₂Te₃ films by an MOCVD process. *J. Mater. Chem. A* **2**, 8215 (2014).
- Wang, M.-X. *et al.* The Coexistence of Superconductivity and Topological Order in the Bi₂Se₃ Thin Films. *Science*. **336**, 52–55 (2012).
- Hasan, M. Z. & Kane, C. L. Colloquium : Topological insulators. *Rev. Mod. Phys.* **82**, 3045–3067 (2010).
- Nakatsuji, S. *et al.* Spontaneous Hall Effect in the Spin Liquid Phase of Pr₂Ir₂O₇. *J. Phys. Conf. Ser.* **320**, 012056 (2011).
- Ueda, K. *et al.* Variation of Charge Dynamics in the Course of Metal-Insulator Transition for Pyrochlore-Type Nd₂Ir₂O₇. *Phys. Rev. Lett.* **109**, 136402 (2012).
- Sushkov, A. B. *et al.* Optical evidence for a Weyl semimetal state in pyrochlore Eu₂Ir₂O₇. *arXiv:1507.01038* 1–4 (2015).
- Yang, B. J. & Kim, Y. B. Topological insulators and metal-insulator transition in the pyrochlore iridates. *Phys. Rev. B* **82**, 085111 (2010).
- Wan, X., Turner, A. M., Vishwanath, A. & Savrasov, S. Y. Topological semimetal and Fermi-arc surface states in the electronic structure of pyrochlore iridates. *Phys. Rev. B* **83**, 205101 (2011).
- Matsuhira, K. *et al.* Metal-Insulator Transition in Pyrochlore Iridates Ln₂Ir₂O₇ (Ln=Nd,Sm,Eu). *J. Phys. Soc. Japan* **76**, 043706 (2007).
- Matsuhira, K., Wakeshima, M., Hinatsu, Y. & Takagi, S. Metal-Insulator Transitions in Pyrochlore Oxides Ln₂Ir₂O₇. *J. Phys. Soc. Japan* **80**, 094701 (2011).
- Matsuhira, K., Tokunaga, M., Wakeshima, M., Hinatsu, Y. & Takagi, S. Giant Magnetoresistance Effect in the Metal-Insulator Transition of Pyrochlore Oxide Nd₂Ir₂O₇. *J. Phys. Soc. Japan* **82**, 23706 (2013).
- Yang, B. J. & Nagaosa, N. Emergent topological phenomena in thin films of pyrochlore iridates. *Phys. Rev. Lett.* **112**, 246402 (2014).
- Chu, J.-H. *et al.* Linear magnetoresistance and time reversal symmetry breaking of pyrochlore iridates Bi₂Ir₂O₇. *arXiv*, **1309**, 4750v2 (2013).
- Fujita, T. C. *et al.* Odd-parity magnetoresistance in pyrochlore iridate thin films with broken time-reversal symmetry. *Sci. Rep.* **5**, 9711 (2015).
- Cordfunke, E. H. P. & Meyer, G. The system iridium-oxygen I. Measurements on the volatile oxide of iridium. *Recl. des Trav. Chim. des Pays-Bas* **81**, 495–504 (1962).
- Hinatsu, Y., Doi, Y., Nishimine, H., Wakeshima, M. & Sato, M. Phase transition of the orthorhombic fluorite-related compounds Ln₂IrO₇ (Ln=Pr, Nd, Sm, Eu). *J. Alloys Compd.* **488**, 541–545 (2009).
- Jacob, K. T., Okabe, T. H., Uda, T. & Waseda, Y. Solid-state cells with buffer electrodes for accurate thermodynamic measurements: system Nd-Ir-O. *Electrochim. Acta* **45**, 1963–1971 (2000).
- Heiroth, S. *et al.* Crystallization and grain growth characteristics of yttria-stabilized zirconia thin films grown by pulsed laser deposition. *Solid State Ionics* **191**, 12–23 (2011).
- Humphreys, R. G. *et al.* Physical vapour deposition techniques for the growth of YBa₂Cu₃O₇ thin films. *Supercond. Sci. Technol.* **3**, 38–52 (1990).
- Leitner, J., Voňka, P., Sedmidubský, D. & Svoboda, P. Application of Neumann-Kopp rule for the estimation of heat capacity of mixed oxides. *Thermochim. Acta* **497**, 7–13 (2010).
- O'Neill, H. S. C. & Nell, J. Gibbs free energies of formation of RuO₂, IrO₂, and OsO₂: A high-temperature electrochemical and calorimetric study. *Geochim. Cosmochim. Acta* **61**, 5279–5293 (1997).
- Konings, R. J. M. & Beneš, O. The Thermodynamic Properties of the f-Elements and Their Compounds. I. The Lanthanide and Actinide Metals. *J. Phys. Chem. Ref. Data* **39**, 043102 (2010).
- Krishnamurthy, R., Yoon, Y.-G., Srolovitz, D. J. & Car, R. Oxygen Diffusion in Yttria-Stabilized Zirconia: A New Simulation Model. *J. Am. Ceram. Soc.* **87**, 1821–1830 (2005).

Acknowledgements

Funding for this research was provided by the Center for Emergent Materials at the Ohio State University, an NSF MRSEC (Award Number DMR-1420451). Use of the Advanced Photon Source at Argonne National Laboratory was supported by the U. S. Department of Energy, Office of Science, Office of Basic Energy Sciences, under Contract No. DE-AC02-06CH11357. Thin film X-ray diffraction measurements were provided through The Ohio State University's NanoSystems Laboratory. BDE would like to acknowledge Lee Casalena for his help in constructing Figure 6.

Author Contributions

J.C.G. developed the synthesis technique, grew all the samples, collected and analyzed the x-ray diffraction and magnetization data. B.D.E. and R.E.W. collected and analyzed the STEM and EDX data. R.M. performed the Rietveld refinement analysis of powder diffraction data. S.R.D. collected and analyzed the magnetization data. P.M.W. supervised analysis of bulk samples. D.W.M. supervised STEM measurements and analysis. F.Y.Y. supervised the project. All authors contributed to writing the manuscript.

Additional Information

Supplementary information accompanies this paper at <http://www.nature.com/srep>

Competing financial interests: The authors declare no competing financial interests.

How to cite this article: Gallagher, J. C. *et al.* Epitaxial growth of iridate pyrochlore Nd₂Ir₂O₇ films. *Sci. Rep.* **6**, 22282; doi: 10.1038/srep22282 (2016).



This work is licensed under a Creative Commons Attribution 4.0 International License. The images or other third party material in this article are included in the article's Creative Commons license, unless indicated otherwise in the credit line; if the material is not included under the Creative Commons license, users will need to obtain permission from the license holder to reproduce the material. To view a copy of this license, visit <http://creativecommons.org/licenses/by/4.0/>